

First-Principles Prediction of New Electrides with Nontrivial Band Topology Based on One-Dimensional Building Blocks

Changwon Park,^{1,2} Sung Wng Kim,^{3,*} and Mina Yoon^{1,2,†}

¹Center for Nanophase Materials Sciences, Oak Ridge National Laboratory, Oak Ridge, Tennessee 37831, USA

²Department of Physics and Astronomy, University of Tennessee, Knoxville, Tennessee 37916, USA

³Department of Energy Science, Sungkyunkwan University, 300 Cheoncheon-dong, Jangan-gu, Suwon, Gyeonggi-do 440-746, South Korea



(Received 6 June 2017; published 8 January 2018)

We introduce a new class of electrides with nontrivial band topology by coupling materials database searches and first-principles-calculations-based analysis. Cs_3O and Ba_3N are for the first time identified as a new class of electrides, consisting of one-dimensional (1D) nanorod building blocks. Their crystal structures mimic $\beta\text{-TiCl}_3$ with the position of anions and cations exchanged. Unlike the weakly coupled nanorods of $\beta\text{-TiCl}_3$, Cs_3O and Ba_3N retain 1D anionic electrons along the hollow interrod sites; additionally, a strong interrod interaction in Cs_3O and Ba_3N induces band inversion in a 2D superatomic triangular lattice, resulting in Dirac-node lines. The new class of electrides can serve as a prototype for new electrides with a large cavity space that can be utilized for various applications such as gas storage, ion transport, and metal intercalation.

DOI: [10.1103/PhysRevLett.120.026401](https://doi.org/10.1103/PhysRevLett.120.026401)

The electride, named by Dye *et al.* in 1978 [1], first described a synthesized solid film of alkali metal chelated by 2,2,2-cryptand, where electrons are not bound to the constituent components (metals or molecules), but instead are localized in atomic-scale cavities of the film [2]. The concept of non-nuclear-bound electrons (or anionic electrons) was first validated in an alkali metal dissolved ammonia, where the clear blue color of the solution was attributed to a “metallic fog” [3] that are electrons surrounded by solvent molecules [4,5], and anionic electrons have been further confirmed in various solids by a sequence of experimental [6–8] and theoretical [9–11] analyses. The availability of highly mobile non-nucleus-bound electrons makes electrides promising for optoelectric and catalytic applications.

Room-temperature stable electrides became accessible only recently with $\text{Ca}_{24}\text{Al}_{28}\text{O}_{64}$ [12]. Sequentially, a two-dimensional (2D) room-temperature stable electride of Ca_2N [13] has been synthesized. Both of these electrides offer high electron-donating powers as reflected in the Pinacol coupling reaction [14], ammonia synthesis [15], and trifluoromethylation [16]. In particular, Ca_2N serves as a prototypical material for binary [17–20] layered electrides using computational searches based on a database [21] and evolutionary algorithms [22–24], which provided possible electride candidates and design principles [21–24].

Once a new electride is found, the most straightforward extension for the next electride is to combinatorially change its elements but retain its crystal symmetry. Since its rediscovery as a two-dimensional electride, many electrides with anti- CdCl_2 structures have been suggested [22–24]. So far, however, those electrides, either experimentally

synthesized or theoretically predicted, are in a limited class with respect to crystal symmetry and chemical groups. Therefore, an alternative scheme for the discovery of a new class of electrides is highly desirable.

In this Letter, we report a new class of electrides based on one-dimensional (1D) nanorod building blocks by coupling materials database searches and first-principles-calculations-based analysis. This new class of electrides has crystal structures that mimic $\beta\text{-TiCl}_3$ with the position of anions and cations exchanged. Unlike the weakly coupled nanorods of $\beta\text{-TiCl}_3$, Cs_3O and Ba_3N retain 1D anionic electrons along the interrod hollow sites; additionally, strong interrod interaction in Cs_3O and Ba_3N induces band inversion in a 2D superatomic triangular lattice, resulting in Dirac nodal lines. The availability of the large cavity space with metallic electrons makes the new electrides very interesting for applications such as gas storage, ion transport, and metal intercalation. Moreover, our work demonstrates how the concept of antistructures can be developed to discover new electrides.

Our first-principles calculations and analysis are based on the density functional theory employing the Perdew-Burke-Ernzerhof (PBE) exchange-correlation functional [25] and the projector augmented wave method for ionic potentials [26] as implemented in the Vienna *ab initio* simulation package (VASP) [27]. We also employed a van der Waals (vdW) scheme [28] corrected on top of the PBE functional to elucidate the role of vdW interactions in stabilizing structures and to confirm the accuracy of PBE structure optimization. The energy cutoff of the plane wave basis was 400 eV, and $18 \times 18 \times 1$ k points including the Γ point were sampled

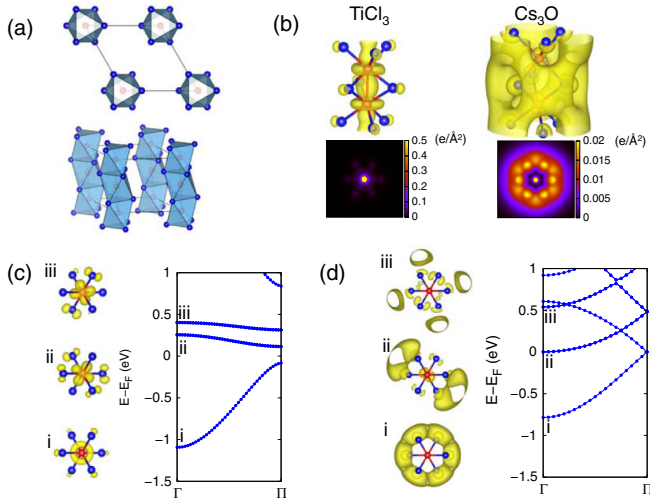


FIG. 1. (a) Crystal structure of TiCl_3 (Cs_3O) in top and side view. Red and blue balls correspond to Ti (O) and Cl (Cs), respectively. (b) Isosurfaces (top) and axially integrated (bottom) anionic electron density (see text) of isolated TiCl_3 and Cs_3O rod. One-dimensional band structure and selected wave functions at the Γ point are shown for (c) TiCl_3 and (d) Cs_3O .

for converged charge densities. All atoms were fully relaxed with a force criterion of $0.02 \text{ eV}/\text{\AA}$.

Our exploration of new electrides started from the available crystal database [29]. We sequentially applied aggressive criteria to the database, such as positive oxidation numbers, low band gaps, excluding d - or f -electron systems within binary crystals, and discovered Cs_3O as a candidate new electride with apparent 1D crystal structure of $P6_3/mcm$ symmetry [Fig. 1(a)]. This material already has been experimentally synthesized [30] but never identified as an electride. The theoretical phase diagram of the Cs—O system is replotted from the materials' database [29] in the Supplemental Material [31]. In this quasi-1D crystal, six Cs atoms connected to a central O atom form a trigonal antiprismatic unit that is the basis of the 1D array of face-sharing octahedrons. The nanorods are closely packed into a 2D triangular lattice with experimental lattice constants of $a = 8.78 \text{ \AA}$ and $c = 7.52 \text{ \AA}$ [30]. Note that our lattice constants based on PBE functional calculations ($a = 8.81 \text{ \AA}$ and $c = 7.53 \text{ \AA}$) are in great agreement with the experimental values of $\sim 0.3\%$ and $\sim 0.1\%$ errors for a and c , respectively.

Many transition metal trihalides such as $\beta\text{-TiCl}_3$ [32], TiI_3 , ZrCl_3 , and MoBr_3 [33] share the crystal structure of Cs_3O with some differences in their intrarod atomic arrangement. $\beta\text{-TiCl}_3$ has a uniform intrarod metal-metal distance, similar to that of Cs_3O , whereas most transition metal trihalides have alternating bond lengths with an additional degree of freedom for interrod stacking [34]. Besides their structural similarities, the stark difference is on the exchange of cation and anion locations; that is, Cs_3O can be categorized as an anti- TiCl_3 .

Based on the formal charges of individual atoms, the charge states of TiCl_3 and Cs_3O can be expressed as $\text{Ti}^{4+}(\text{Cl}^-)_3e^-$ and $(\text{Cs}^+)_3\text{O}^{2-}e^-$, which anticipates one free electron per formula unit with no explicit binding to any ions. The unit cell of the crystal contains two formula units, and the bands near the Fermi levels are identified as the states occupied by the two excess electrons. Figure 1(b) depicts the spatial distributions of the excess electrons of isolated rods of TiCl_3 and Cs_3O by integrating two electrons distributed over the near Fermi level bands. The isolated Cs_3O rod retains the octahedral arrangement of the bulk counterpart, while a dimerized octahedron becomes more favorable [by 23 meV per formula unit (f.u.)] for an isolated TiCl_3 rod. The excess electrons of the Cs_3O rod reside along the rod circumference. In contrast, the excess electrons of the TiCl_3 rod are distributed mostly along the Ti atoms centered at the rod. The electrons localized along the metal atoms are attributed to the rich 1D physics of transition metal trihalide, including Peierls distortion, magnetic ordering [33], and topological excitation gap [35].

We further analyze the electronic properties of the 1D rods. Figures 1(c) and 1(d) present the 1D band structures of TiCl_3 and Cs_3O , respectively, along the stacking of octahedral units. For the TiCl_3 rod, the integration of band i in Fig. 1(c) corresponds to the excess electrons visualized in Fig. 1(b), the highly dispersive d_{z^2} -orbital electrons of Ti atoms. Two lowest unoccupied bands, ii and iii , are d_{xy} and $d_{x^2-y^2}$ orbitals that have a slight band dispersion due to the small spatial overlaps between Ti atoms. For Cs_3O , the circumferential states composed mainly of Cs s orbital form the low-energy band i of Fig. 1(d). The d_{z^2} band of TiCl_3 induces an energy gap of $\sim 0.9 \text{ eV}$ at the zone boundary, stemming from the dimerization of Ti atoms. On the other hand, Cs_3O bands are folded at the zone boundary without any energy gaps (no dimerization), where each band is characterized by the number of nodes in the circumferential direction. Given the approximate nature of the cylindrical symmetry, the circular part of the wave functions can be expressed as $e^{im\theta}$ ($m = 0, \pm 1, \pm 2$) with θ and m being the polar angle and the number of nodes, respectively. The i , ii , and iii bands in Fig. 1(d) are characterized with $m = 0, \pm 1$ and ± 2 , respectively, the ii and iii bands are doubly degenerated. Here we present the charge densities of only one of the degenerated states at the Γ point. As discussed later, the low-lying $m = 0$ and $m = \pm 1$ states serve as a good basis for superatoms that compose Cs_3O bulk.

Next, we elucidate the properties of the Cs_3O bulk crystals in comparison to those of the well-investigated TiCl_3 crystal [32]. Despite the similarities in their crystal structures, the exchange of anion and cation locations essentially make a qualitative difference in their basic properties. Figure 2(a) highlights the cylindrically integrated electron densities of each rod, $\rho(r) \equiv \int_0^c \int_0^{2\pi} \rho(\vec{r}) r d\theta dz$, where r is the radius of a cylinder and c is the lattice constant of the rod axial direction. The solid black lines denote the radial distances of each

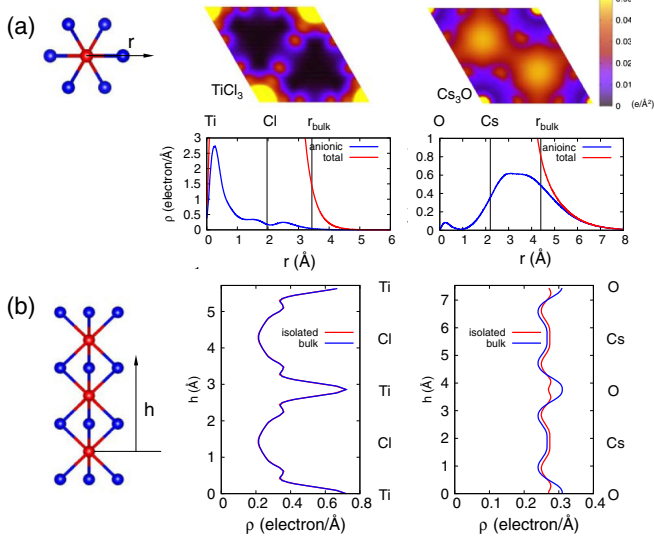


FIG. 2. (a) Axially integrated anionic electron density of bulk TiCl_3 (upper left) and Cs_3O (upper right) and cylindrically integrated electron density $\rho(r) \equiv \int_0^c \int_0^{2\pi} \rho(\vec{r}) r d\theta dz$ of isolated rods, where r is the radius of a cylinder and c is the lattice constant along the axial direction. Anionic and total electron densities of TiCl_3 (lower left) and Cs_3O (lower right) are plotted in red and blue, respectively. The position of each element and the bulk equilibrium bond length (r_{bulk}) are shown. (b) Planar-averaged anionic electron densities of isolated rods (red) and bulks (blue). For TiCl_3 , both densities are not distinguished in the shown scale.

chemical element and the halved equilibrium bulk lattice constant ($a/2$, r_{bulk}). The TiCl_3 bulk has highly concentrated anionic electrons around Ti atoms, which are drastically reduced at Cl and completely diminished at $r > r_{\text{bulk}}$. In stark contrast, the anionic electrons of Cs_3O , with the highest amount in the middle of Cs and r_{bulk} positions, essentially govern the total charge density at the large distance, $r > r_{\text{bulk}}$. The formation of bonding between partially ionized cations [36] is a common feature of solid electrides, where bond lengths between cations are typically somewhat larger than the bond lengths of elemental metals, which results in stable cavity spaces. This feature is manifested in the in-planar cross section of anionic electron charge densities in Fig. 2(a), where Cs_3O has the highest charge density at the cavity space in between the rods, whereas TiCl_3 has the maximum anionic electron density centered at the Ti metal sites. The weak interrod interaction between the nanorods of TiCl_3 is governed by vdW interaction, as the vdW corrected PBE calculations closely predict lattice constants ($a = 6.32 \text{ \AA}$ and $c = 5.82 \text{ \AA}$) that are in good agreement with the experimental values ($a = 6.27 \text{ \AA}$ and $c = 5.82 \text{ \AA}$); note that PBE without vdW correction results in a larger deviation ($a = 6.87 \text{ \AA}$ and $c = 5.72 \text{ \AA}$). The anionic charges of TiCl_3 , highly localized at Ti d_{z^2} orbitals, along the axial direction remain intact by forming bulk crystals from the isolated rods [Fig. 2(b)]. For Cs_3O ,

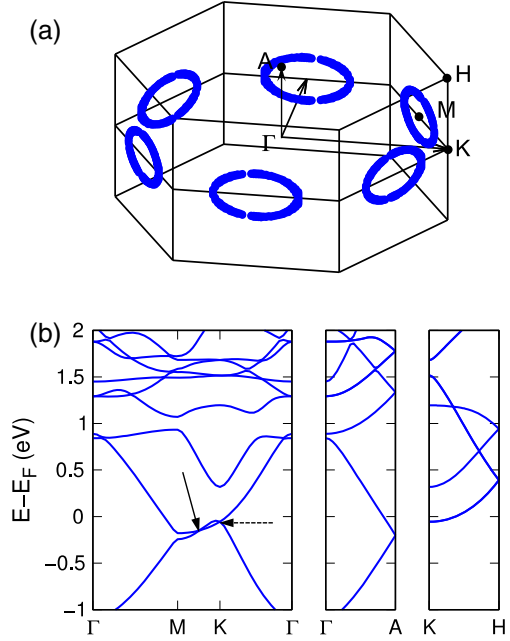


FIG. 3. (a) Brillouin zone and node lines of Cs_3O . (b) Band structure of Cs_3O along high symmetry lines. Nodal point and degeneracy at the K point are denoted by solid and dashed arrows, respectively.

anionic charges, bound to the circumferential states of each rods, accumulate at the interrod hollow sites near the oxygen atoms, where the orbital overlaps between the Cs atoms of each rod become maximum, for the bulk crystal.

Next we focus on analyzing the electronic band structures of bulk Cs_3O . Figure 3(a) presents the band structures along the high symmetry points denoted in Fig. 3(b). The dimensional anisotropy of Cs_3O is embedded in the in-planar 2D and axial 1D band structures. Along the axial direction, bands near the Fermi level are composed of 1D parabolic bands of different circumferential states folded at the zone boundary, where the relative energy levels of each circumferential state and the band dispersion strongly depend on the planar crystal momentum. In stark contrast, the axial band structure of an isolated TiCl_3 rod is unperturbed by the formation of bulk crystals. The in-plane bands show rich features including highly dispersive bands near the Fermi level and nontrivial band inversion, in stark contrast to the flat bands of TiCl_3 stemming from the negligible interrod interactions. In particular, we try to unravel the origin of the two band crossings near the Fermi level. The crystal symmetry of the lattice results in the doubly degenerate point at the K point (dashed arrow). Specifically, D_{3h} symmetry along K-H results in the degeneracy of two p -like (p_x and p_y) states. On the other hand, the degeneracy located in between the M and K points (solid arrow) turns out to be the remnant of the band inversion between the s - and p -like states, as discussed below.

We monitor the band inversion features by gradually reducing the interrod interaction. The top panel of Fig. 4

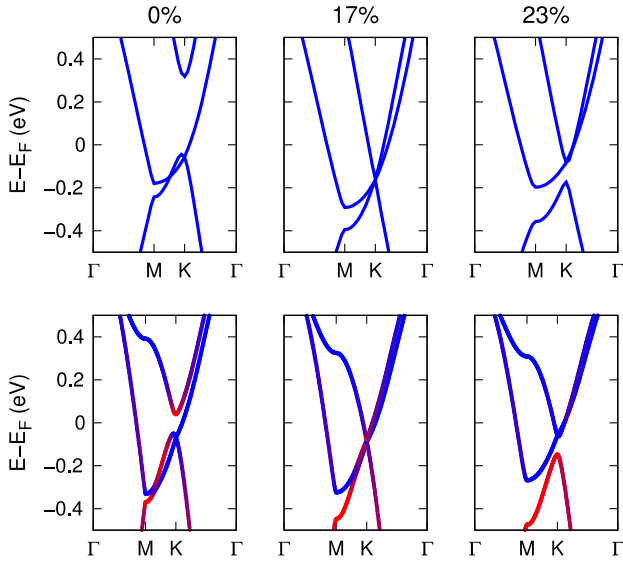


FIG. 4. Biaxial strain-dependent band structure (top panels) and corresponding three-band tight-binding model band structures (bottom panels). Hopping parameters of the zero strain tight-binding model are scaled by 0.9 and 0.8 for 17% and 23% biaxial strain, respectively.

presents first-principles band structures with biaxial strain (0%, 17%, and 23%). Under the biaxial strains, the interrod distance increases while leaving the intrarod structures intact (e.g., Cs—O bond lengths remain unchanged); thus, any changes in the band structure can be solely assigned to the change of interrod interaction. To acquire a clear physical picture, we construct a three-band tight-binding model based on $m = 0$ (s -like) and $m = \pm 1$ (p -like) states that effectively represent the near-Fermi level states. The tight-binding (TB) band structures are presented on the bottom panel of Fig. 4, where the red and blue colors represent s and p bands, respectively. The Slater-Koster hopping parameters [37] between the superatomic basis set of s , p_x , and p_y orbitals on the triangular lattice are listed in Table I. The hopping parameters of the strained systems are scaled by 0.9 (0.8) for 17% (23%) of biaxial strain. These parameters well capture the key features of first-principles band structures, and furthermore the TB bands unambiguously demonstrate the s - p band inversion (see the bottom panel of Fig. 4). The s and p bands are separated in a weakly interacting rod system (under 23% strain). As the

TABLE I. Hopping parameters fitted to first-principles band structures with the basis set of s , p_x , and p_y orbitals, into nearest neighbors (n.n.) and next nearest neighbors (n.n.n.). The onsite energy is larger for p orbitals and their difference Δ is also shown.

Hopping	s - s (n.n)	s - p (n.n)	$pp\sigma$ (n.n)	$pp\pi$ (n.n)	s - s (n.n.n)	Δ
Energy (eV)	-0.17	-0.19	-0.15	0.05	0.03	0.88

interrod interaction becomes stronger, the two bands move closer to each other and the band inversion appears at 17% strain. At the optimized structure (under no strain) the s - p band inversion occurs at the degeneracy point in between M and K points.

Band inversion is one of the characteristic features of nontrivial bands [38–40]. Specifically, band inversion between atomic s and p (or d) states was the prerequisite for Dirac-node line materials [38], recently reported for simple elemental metals such as Be [39], Ca, Sr, and Yb [40]. We confirm that the principle is valid for our superatomic s - and p -band system. The degeneracy points between the M and K points presented in the 2D band [Fig. 3(a)] are connected in the 3D Brillouin zone (BZ) and form a loop encircling the M points, thus creating node lines in between M and K points. Figure 3(b) shows the circularlike node lines around M points. The loops delineate the boundaries between the s and p band. These Dirac node line loops are topologically protected, and robust against any perturbations that preserve both time-reversal and inversion symmetries [38].

Using Cs_3O as a prototype electride, we further identify Ba_3N (see the phase diagram of Ba—N in SM), in the crystal database [29], with the symmetry of Cs_3O as a new electride. Based on the formal charges it can be written as $(\text{Ba}^{2+})_3 \text{N}^{3-} 3e^-$. Figure 5 presents 2D in-planar (left) and 1D axial (right) band structures. The 1D band shows a highly dispersive, parabolic band, similar to that of Cs_3O . The seemingly triply degenerated states at the K point with energy of -0.6 eV are composed of p_x - and p_y -like states and s -like states. In fact, the band structure of the equilibrium crystal structure bears some resemblance to the Cs_3O band under 17% biaxial strain in Fig. 3(d), indicating that interrod interaction is effectively weaker in Ba_3N than in Cs_3O . Ba_3N contains two additional bands, at energies -0.3 and -1.6 eV, which are relatively flat in the Γ - M - K - Γ plane. The partially flat bands originate from the hybridization between Ba p and d orbitals. Because of the weak interrod interaction for those states, their energy and dispersion along the axial direction remain essentially unaffected by the formation of bulk from the isolated rods (right panel of Fig. 5).

We confirmed that Cs_3O and Ba_3N are the only available electrides with anti- TiCl_3 structure in the materials database. However, there is a wide class of k -ary compounds with structures similar to anti- TiCl_3 . For example, the parent form of Ba_3N is intact by intercalating with alkali metals Ba_3NLi [41] and NaBa_3N [42], as they were already experimentally synthesized. This suggests a strategy for discovering new potential 1D electrides not found in the database: Starting from known ternary compounds having anti- TiCl_3 frameworks, we can computationally remove intercalated cations and check their stability. We can further utilize the new prototypical electride by theoretically exploring alternative elements and formal charge states. The availability of the

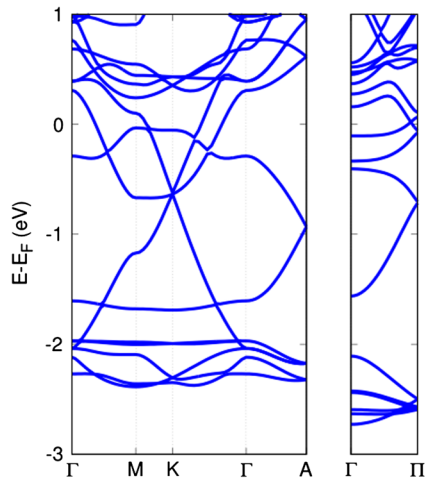


FIG. 5. (left) Bulk band structure of Ba_3N and (right) one-dimensional band structure of the isolated Ba_3N rod.

large cavity space with metallic electrons makes the new electrides very interesting for applications such as gas storage, ion transport, and metal intercalation. Moreover, we demonstrate how the concept of antistructures can be developed to discover new electrides.

In summary, we present Cs_3O and Ba_3N as new electrides with the intriguing $(2 + 1)$ -dimensional properties using an approach that combines materials database searches and first-principles calculations. The new class of electrides can be categorized as antisite $\beta\text{-TiCl}_3$, a well-established material of 1D physics. The anionic electrons are highly concentrated in the interrod cavity space due to the formation of a 2D superatomic triangular lattice. Hopping between the inter-superatomic orbitals induces an s - p band inversion, which results in topological node lines.

Research was conducted at the Center for Nanophase Materials Sciences (CNMS), which is a DOE Office of Science User Facility. We also acknowledge support by the U.S. Department of Energy, Office of Science, Basic Energy Sciences (BES), Materials Sciences and Engineering Division, for performing first-principles calculations, CNMS for first-principles data analysis, and by the Creative Materials Discovery Program through the National Research Foundation of Korea (NRF) funded by the Ministry of Science, ICT and Future Planning (NRF-2016M3D1A1919181) for performing database searches and analysis. Computing resources were provided by the National Energy Research Scientific Computing Center, which is supported by the Office of Science of the U.S. Department of Energy under Contract No. DE-AC02-05CH11231. The authors acknowledge useful discussions with J. Lasseter and J. Park.

This manuscript has been authored by UT-Battelle, LLC under Contract No. DE-AC05-00OR22725 with the U.S. Department of Energy. The United States Government retains and the publisher, by accepting the article for publication,

acknowledges that the United States Government retains a nonexclusive, paid-up, irrevocable, world-wide license to publish or reproduce the published form of this manuscript, or allow others to do so, for United States Government purposes. The Department of Energy will provide public access to these results of federally sponsored research in accordance with the DOE Public Access Plan [43].

*kimsungwng@skku.edu

†myoon@ornl.gov

- [1] J. L. Dye, M. R. Yemen, M. G. DaGue, and J.-M. Lehn, Optical spectra of alkali metal anion and electride films, *J. Chem. Phys.* **68**, 1665 (1978).
- [2] J. L. Dye, Electrons as anions, *Science* **301**, 607 (2003).
- [3] F. M. G. Johnson and N. T. M. Wilsmore, Electrode potentials in liquid ammonia, *Trans. Faraday Soc.* **3**, 70 (1907).
- [4] C. A. Kraus, Solutions of metals in non-metallic solvents; general properties of metals in liquid ammonia, *J. Am. Chem. Soc.* **29**, 1557 (1907).
- [5] C. A. Kraus, Solutions of metals in non-metallic solvents; IV. Material effects accompanying the passage of an electrical current through solutions of metals in ammonia. Migration experiments, *J. Am. Chem. Soc.* **30**, 1323 (1908).
- [6] S. B. Dawes, D. L. Ward, R. H. Huang, and J. L. Dye, First electride crystal structure, *J. Am. Chem. Soc.* **108**, 3534 (1986).
- [7] R. H. Huang, M. K. Faber, K. J. Moeggenborg, D. L. Ward, and J. L. Dye, Structure of $\text{K}+(\text{cryptand}[2.2.2])$ electride and evidence for trapped electron pairs, *Nature (London)* **331**, 599 (1988).
- [8] M. J. Wagner, R. H. Huang, J. L. Eglin, and J. L. Dye, An electride with a large six-electron ring, *Nature (London)* **368**, 726 (1994).
- [9] J. L. Dye, Anionic electrons in electrides, *Nature (London)* **365**, 10 (1993).
- [10] D. J. Singh, H. Krakauer, C. Haas, and W. E. Pickett, Theoretical determination that electrons act as anions in the electride $\text{Cs}+(15\text{-crown-5})_2\text{e}^-$, *Nature (London)* **365**, 39 (1993).
- [11] J. L. Dye, M. J. Wagner, G. Overney, R. H. Huang, T. F. Nagy, and D. Tománek, Cavities and channels in electrides, *J. Am. Chem. Soc.* **118**, 7329 (1996).
- [12] S. Matsuishi, Y. Toda, M. Miyakawa, K. Hayashi, T. Kamiya, M. Hirano, I. Tanaka, and H. Hosono, High-density electron anions in a nanoporous single crystal: $[\text{Ca}_{24}\text{Al}_{28}\text{O}_{64}]_4^{4+}(4\text{e}^-)$, *Science* **301**, 626 (2003).
- [13] K. Lee, S.-W. Kim, Y. Toda, S. Matsuishi, and H. Hosono, Dicalcium nitride as a two-dimensional electride with an anionic electron layer, *Nature (London)* **494**, 336 (2013).
- [14] H. Buchhammagari, Y. Toda, M. Hirano, H. Hosono, D. Takeuchi, and K. Osakada, Room temperature-stable electride as a synthetic organic reagent: Application to pinacol coupling reaction in aqueous media, *Org. Lett.* **9**, 4287 (2007).
- [15] M. Kitano, Y. Inoue, Y. Yamazaki, F. Hayashi, S. Kanbara, S. Matsuishi, T. Yokoyama, S.-W. Kim, M. Hara, and H. Hosono, Ammonia synthesis using a stable electride as an

- electron donor and reversible hydrogen store, *Nat. Chem.* **4**, 934 (2012).
- [16] S. Choi, Y. J. Kim, S. M. Kim, J. W. Yang, S.-W. Kim, and E. J. Cho, Hydrotrifluoromethylation and iodotrifluoromethylation of alkenes and alkynes using an inorganic electride as a radical generator, *Nat. Commun.* **5**, 4881 (2014).
- [17] Y. Ma, M. Eremets, A. R. Oganov, Y. Xie, I. Trojan, S. Medvedev, O. Lyakhov, M. Valle, and V. Prakapenka, Transparent dense sodium, *Nature (London)* **458**, 182 (2009).
- [18] M. Marqués, G. J. Ackland, L. F. Lundegaard, G. Stinton, R. J. Nelmes, M. I. McMahon, and J. Contreras-García, Potassium under Pressure: A Pseudobinary Ionic Compound, *Phys. Rev. Lett.* **103**, 115501 (2009).
- [19] M. Gatti, I. V. Tokatly, and A. Rubio, Sodium: A Charge-Transfer Insulator at High Pressures, *Phys. Rev. Lett.* **104**, 216404 (2010).
- [20] M. Marqués, M. I. McMahon, E. Gregoryanz, M. Hanfland, C. L. Guillaume, C. J. Pickard, G. J. Ackland, and R. J. Nelmes, Crystal Structures of Dense Lithium: A Metal-Semiconductor-Metal Transition, *Phys. Rev. Lett.* **106**, 095502 (2011).
- [21] T. Tada, S. Takemoto, S. Matsuishi, and H. Hosono, High-throughput *ab initio* screening for two-dimensional electride materials, *Inorg. Chem.* **53**, 10347 (2014).
- [22] Y. Tsuji, P. L. V. K. Dasari, S. F. Elatresh, R. Hoffmann, and N. W. Ashcroft, Structural diversity and electron confinement in Li₄N: Potential for 0-D, 2-D, and 3-D electrides, *J. Am. Chem. Soc.* **138**, 14108 (2016).
- [23] Y. Zhang, H. Wang, Y. Wang, L. Zhang, and Y. Ma, Computer-Assisted Inverse Design of Inorganic Electrides, *Phys. Rev. X* **7**, 011017 (2017).
- [24] W. Ming, M. Yoon, M.-H. D. K. Lee, and S.-W. Kim, First-principles prediction of thermodynamically stable two-dimensional electrides, *J. Am. Chem. Soc.* **138**, 15336 (2016).
- [25] J. P. Perdew, K. Burke, and M. Ernzerhof, Generalized Gradient Approximation Made Simple, *Phys. Rev. Lett.* **77**, 3865 (1996).
- [26] G. Kresse and D. Joubert, From ultrasoft pseudopotentials to the projector augmented-wave method, *Phys. Rev. B* **59**, 1758 (1999).
- [27] G. Kresse and J. Furthmüller, Efficient iterative schemes for *ab initio* total-energy calculations using a plane-wave basis set, *Phys. Rev. B* **54**, 11169 (1996).
- [28] A. Tkatchenko and M. Scheffler, Accurate Molecular van Der Waals Interactions from Ground-State Electron Density and Free-Atom Reference Data, *Phys. Rev. Lett.* **102**, 073005 (2009).
- [29] A. Jain, S. P. Ong, G. Hautier, W. Chen, W. D. Richards, S. Dacek, S. Cholia, D. Gunter, D. Skinner, G. Ceder, and K. A. Persson, The Materials Project: A materials genome approach to accelerating materials innovation, *APL Mater.* **1**, 011002 (2013).
- [30] K.-R. Tsai, P. M. Harris, and E. N. Lassetre, The crystal structure of tricesium monoxide, *J. Phys. Chem.* **60**, 345 (1956).
- [31] See Supplemental Material at <http://link.aps.org/supplemental/10.1103/PhysRevLett.120.026401> for the phase diagram of Cs – O system.
- [32] G. Natta, P. Corradini, I. W. Bassi, and L. Porri, Polymorphism of crystalline titanium trichloride, *Rend. Accad. Naz. Lincei* **24**, 121 (1958).
- [33] J. Lin and G. J. Miller, Dimensional diversity in transition metal trihalides, *Inorg. Chem.* **32**, 1476 (1993).
- [34] S. Merlino, L. Labella, F. Marchetti, and S. Toscani, Order-disorder transformation in RuBr₃ and MoBr₃: A two-dimensional ising model, *Chem. Mater.* **16**, 3895 (2004).
- [35] W. J. L. Buyers, R. M. Morra, R. L. Armstrong, M. J. Hogan, P. Gerlach, and K. Hirakawa, Experimental Evidence for the Haldane Gap in a Spin-1 nearly Isotropic, Antiferromagnetic Chain, *Phys. Rev. Lett.* **56**, 371 (1986).
- [36] A. Simon, Alkali metal suboxides: Intermediates between salts and metals, *J. Solid State Chem.* **27**, 87 (1979).
- [37] D. A. Papaconstantopoulos and M. J. Mehl, The Slater-Koster tight-binding method: a computationally efficient and accurate approach, *J. Phys. Condens. Matter* **15**, R413 (2003).
- [38] H. Weng, Y. Liang, Q. Xu, R. Yu, Z. Fang, X. Dai, and Y. Kawazoe, Topological node-line semimetal in three-dimensional graphene networks, *Phys. Rev. B* **92**, 045108 (2015).
- [39] R. Li, H. Ma, X. Cheng, S. Wang, D. Li, Z. Zhang, Y. Li, and X.-Q. Chen, Dirac Node Lines in Pure Alkali Earth Metals, *Phys. Rev. Lett.* **117**, 096401 (2016).
- [40] M. Hirayama, R. Okugawa, T. Miyake, and S. Murakami, Topological Dirac nodal lines and surface charges in fcc alkaline earth metals, *Nat. Commun.* **8**, 14022 (2017).
- [41] V. Smetana, V. Babizhetskyy, G. V. Vajenine, and A. Simon, Synthesis and crystal structure of LiBa₂N and identification of LiBa₃N, *J. Solid State Chem.* **180**, 1889 (2007).
- [42] P. E. Rauch and A. Simon, The new subnitride NaBa₃N; an extension of alkali metal suboxide chemistry, *Angew. Chem., Int. Ed. Engl.* **31**, 1519 (1992).
- [43] <http://energy.gov/downloads/doepublic-access-plan>.